





# Magnetically tunable supercurrent in dilute magnetic topological insulator-based Josephson junctions

Received: 31 August 2023

Accepted: 14 March 2024

Published online: 01 April 2024

 Check for updates

Pankaj Mandal <sup>1,2</sup>✉, Soumi Mondal<sup>1,2</sup>, Martin P. Stehno<sup>1,2</sup>, Stefan Ilić<sup>3</sup>, F. Sebastian Bergeret <sup>3,4</sup>, Teun M. Klapwijk<sup>1,5</sup>, Charles Gould <sup>1,2</sup>✉ & Laurens W. Molenkamp <sup>1,2</sup>✉

A superconductor, when exposed to a spin-exchange field, can exhibit spatial modulation of its order parameter, commonly referred to as the Fulde–Ferrell–Larkin–Ovchinnikov state. Such a state can be induced by controlling the spin-splitting field in Josephson junction devices, allowing access to a wide range of the phase diagram. Here we demonstrate that a Fulde–Ferrell–Larkin–Ovchinnikov state can be induced in Josephson junctions based on the two-dimensional dilute magnetic topological insulator (Hg,Mn)Te. We do this by observing the dependence of the critical current on the magnetic field and temperature. The substitution of Mn dopants induces an enhanced Zeeman effect, which can be controlled with high precision by using a small external magnetic field. We observe multiple re-entrant behaviours of the critical current as a response to an in-plane magnetic field, which we assign to transitions between ground states with a phase shifted by  $\pi$ . This will enable the study of the Fulde–Ferrell–Larkin–Ovchinnikov state in much more accessible experimental conditions.

In their pioneering papers, Fulde and Ferrell, and Larkin and Ovchinnikov, predicted the existence of an inhomogeneous state now carrying their names (FFLO) when a superconductor is exposed to a spin-exchange field<sup>1,2</sup>. The FFLO state is a consequence of the interplay between this exchange splitting (or, more generally, any spin-splitting field such as a Zeeman field) in the conduction band and the singlet-state Cooper pairs of the superconductor: the pairing state acquires a finite momentum proportional to  $E_z/v_F$ , where  $E_z$  is the Zeeman energy and  $v_F$  is the Fermi velocity. This, in turn, leads to a spatially oscillating order parameter. The initial observation of an FFLO state<sup>3</sup> in the superconductor  $\kappa$ -(BEDT-TTF)<sub>2</sub>Cu(NCS)<sub>2</sub> (BEDT-TTF=bis(ethylene-dithio)tetrathiafulvalene) was restricted to a small temperature and magnetic field range. A recent flurry of activities has shown the same behaviour in various other systems<sup>4–7</sup> that are intrinsic bulk superconductors. A state

analogous to the FFLO state can occur in hybrid superconductor systems, where superconducting correlations in a non-superconducting material are induced by proximity in a spin-splitting field. The latter can be caused by an external field via Zeeman coupling or in ferromagnetic metals (F)<sup>8–10</sup> with an intrinsic exchange field at the Fermi level. As in bulk superconductors, the spin-splitting field leads to pairs of electrons with a finite momentum, which manifest as a spatially oscillating effective order parameter induced in the non-superconducting material defined as  $\Psi(r) = \langle \psi_\uparrow(r)\psi_\downarrow(r) \rangle$ . Notably, whereas the FFLO state in bulk systems is restricted to a narrow range of the phase diagram, the proximity-induced FFLO (pFFLO) state occurs at any field value, allowing for tunability of the device and potentially opening a path towards applicability. While our experiment does not involve scanning probe techniques and thus cannot directly measure the spatial modulation of

<sup>1</sup>Faculty for Physics and Astronomy (EP3), Universität Würzburg, Würzburg, Germany. <sup>2</sup>Institute for Topological Insulators, Würzburg, Germany. <sup>3</sup>Centro de Física de Materiales Centro Mixto CSIC-UPV/EHU, Donostia-San Sebastián, Spain. <sup>4</sup>Donostia International Physics Center, Donostia-San Sebastián, Spain. <sup>5</sup>Kavli Institute of NanoScience, Faculty of Applied Sciences, Delft University of Technology, Delft, the Netherlands. ✉e-mail: [pankaj.mandal@physik.uni-wuerzburg.de](mailto:pankaj.mandal@physik.uni-wuerzburg.de); [gould@physik.uni-wuerzburg.de](mailto:gould@physik.uni-wuerzburg.de); [molenkamp@physik.uni-wuerzburg.de](mailto:molenkamp@physik.uni-wuerzburg.de)

$\Psi(r)$ , we view our observation of a 0– $\pi$  transition and re-entrance superconductivity as a function of both the in-plane magnetic field and the temperature in the same dilute magnetic topological insulator-based weak link device as clear evidence of a pFFLO state.

The pFFLO state is responsible for, among other effects, the transition from a zero phase to a  $\pi$  phase in superconductor–normal–superconductor Josephson junctions (JJs). This is actually a change in the ground state of the junction. It is detected as a re-entrant behaviour of the supercurrent. As a function of continuously varying a parameter, the observed critical current first decreases to zero and then increases again.

However, the measurement of such re-entrant behaviour or a  $\pi$  transition as a function of a single parameter is not sufficient to show a pFFLO state. One also needs to confirm the spatial modulation of  $\Psi(r)$ , which is as shown in Fig. 1c. As such, previous experiments have only hinted at pFFLO, for example, by observing the re-entrant behaviour as a function of the temperature, thickness or magnetic configuration of multilayers, in ferromagnetic weak link junctions<sup>11–16</sup>, where no statement about spatial modulation in a single device can be made, or re-entrance as a function of the in-plane magnetic field in semiconducting weak links<sup>17–20</sup>, where it might originate from simple Fraunhofer-like interference as the field penetrates the cross-section of the only quasi-two-dimensional weak link.

As such, an unambiguous identification of pFFLO behaviour requires a highly tunable device where the re-entrant behaviour can be driven by multiple parameters. In ferromagnetic weak links<sup>9,11–14</sup>, this is not possible as there is no way to substantially tune the strength of the magnetic exchange field within a given device. In non-magnetic semiconducting devices, the Zeeman energy can be tuned by the application of a magnetic field, but the effect is sufficiently weak that the fields that would be needed to reveal pFFLO are so large that they destroy the induced supercurrent. In this Article, we use a dilute magnetic semiconductor weak link to explore the temperature and magnetic field dependence of the pFFLO state.

## Experimental design and characterization

The (Hg,Mn)Te topological insulator weak links used in this study have only a superficial similarity to previous semiconducting weak link JJs studied under an in-plane magnetic field<sup>17</sup>. That study explored the effects of inversion asymmetry in a non-magnetic (and thus low Zeeman splitting) HgTe heterostructure designed to have strong spin–orbit coupling. The spin–orbit coupling strength, which is the product of the Rashba coefficient and the electric field across the quantum well, is strongly dependent on details of the layer stack.

To explore the pFFLO state, our weak link is engineered in the opposite limit from that of ref. 17: we use a highly doped symmetric quantum well in a heterostructure with an electrostatic layout chosen to minimize the electric field across the quantum well and, thus, to produce a negligible Rashba spin–orbit coupling. The strength of the spin–orbit coupling in the sample is determined by Shubnikov–de Haas analysis of the longitudinal resistance<sup>21</sup> of a Hall bar made from the same layer (Supplementary Section 2B). The absence of any beating in the Shubnikov–de Haas data indicates negligible spin–orbit coupling in the transport properties of the layer. Moreover, by substituting a few per cent of the Hg with Mn to utilize the resulting giant effective  $g$  factor<sup>22–25</sup>, we greatly enhance the Zeeman effect. This strongly reduces the magnetic field needed to produce a Zeeman energy  $E_Z = \pi\hbar v_f/2L$ , at which the re-entrant behaviour can be observed. Here,  $L$  is the length of the JJ and  $v_f$  is the Fermi velocity in the semiconductor.

This key difference in the junction material allows us to access a distinct experimental regime. In ref. 17, the large magnetic fields required to reach the 0– $\pi$  transition condition destroy the supercurrent and limit the observations to measuring the differential resistance of the junction in the non-superconducting state. This, in turn, makes temperature-dependent studies impractical. The magnetic dopants

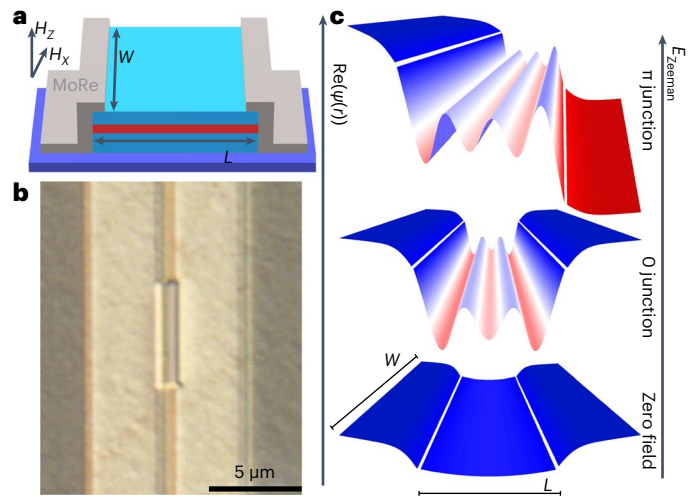


**Fig. 1 | The device layout and a schematic of the spatial modulation of  $\text{Re}(\Psi(r))$ .** **a**, A schematic of a side-contacted JJ with the quantum well indicated in red. The magnetic field directions are indicated in the left corner. **b**, A Nomarski microscopy image of one such investigated JJ. **c**, A schematic of  $\text{Re}(\Psi(r))$  with an increase in the Zeeman energy, for zero field, a 0 junction and a  $\pi$  junction. Darker blue tones indicate more positive values, and darker red more negative, and white marks the zero crossings. The slight curvature in the function in the zero-field case results from the finite decay length for the proximity effect.

incorporated in our weak link reduce the required critical fields by more than one order of magnitude, allowing us to directly measure the magnetic field dependence of the critical current, and this over a substantial temperature range.

The material used for the superconducting leads is MoRe. It has a high upper critical field  $H_{c2}$  and is connected to the quantum well using a side-contact geometry, as shown in the schematic of Fig. 1a. A picture of one of the devices is shown in Fig. 1b. The critical temperature  $T_c$  of the MoRe is 9.6 K, which corresponds to a Bardeen–Cooper–Schrieffer (BCS) gap ( $\Delta$ ) of 1.4 meV. The investigated JJs have a width ( $W$ ) of 5.5  $\mu\text{m}$ , and their length ( $L$ ) varies between 600 and 1,300 nm, all of which are below the mean free path ( $l = 1.7 \mu\text{m}$ ) in the semiconductor. The JJs are studied under both perpendicular-to-plane ( $H_z$ ) and in-plane ( $H_x$ ) magnetic fields orthogonal to the current, as indicated in the device schematic in Fig. 1a. A schematic of the electrical transport measurement scheme is shown in Fig. 2a.

## Results

At zero magnetic field and the base temperature of the dilution fridge, an  $I_c$  of 1.5  $\mu\text{A}$  is observed, as shown in Fig. 2b for the JJ with  $L$  of 950 nm (labelled ‘J2’). Upon applying a perpendicular-to-plane magnetic field  $H_z$ , this junction shows a standard Fraunhofer pattern (Fig. 2c). This confirms a uniform current distribution across the width  $W$  of the JJ<sup>26</sup>. Flux focusing due to the Meissner effect from the long stripe-shaped superconducting leads (4  $\mu\text{m}$  wide) determines the flux<sup>27</sup>.

Figure 2d–k shows the evolution of the  $I(V)$  characteristics as a function of the magnetic field  $H_x$  applied in the plane of the sample and orthogonal to the current direction. As  $H_x$  increases from 0 to 60 mT, we observe a reduction of  $I_c$ . Interestingly, as  $H_x$  is further increased,  $I_c$  begins to grow again until a field of 95 mT is reached, at which it again starts to decrease, reaching zero at 195 mT. These  $I(V)$  characteristics demonstrate re-entrant superconductivity in the JJ at a very low in-plane magnetic field of 60 mT.

This re-entrant behaviour can be seen in more detail by looking directly at  $I_c(H_x)$ , as shown in Fig. 3a. The plotted values of  $I_c$  are extracted from each  $I(V)$  measurement by selecting the current at which a finite voltage criterion of 2  $\mu\text{V}$  is crossed. Given the 60  $\Omega$  resistive state resistance of the junction, this criterion sets a threshold of 30 nA on the

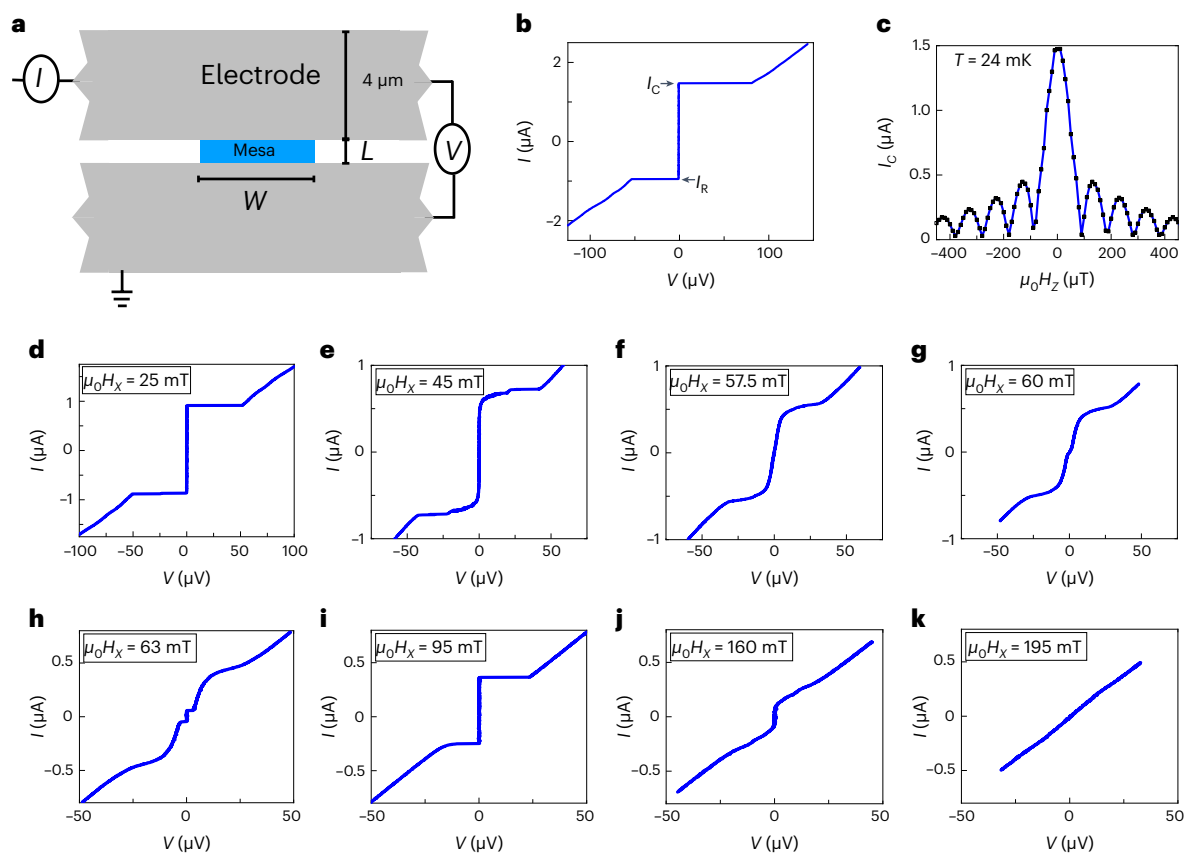


**Fig. 2 | The in-plane magnetic field dependence of the current–voltage characteristic.** **a**, A schematic of the d.c. measurement scheme in the quasi-four-probe configuration. **b**, The  $I(V)$  characteristic at zero magnetic field, indicating the critical current ( $I_C$ ) and the re-trapping current ( $I_R$ ). **c**, The Fraunhofer pattern

of  $I_C(H_x)$ . **d–k**,  $I(V)$  characteristics taken at the various in-plane magnetic fields, indicated in the top of each panel, that are orthogonal to the current direction and at zero perpendicular-to-plane field. The measurements were done at the base temperature of the dilution fridge on sample J2.

$I_C$  sensitivity of the measurement. The red shaded region just above the  $x$  axis in Fig. 3a indicates that the measurements in this 0–30 nA range are below the proper experimental resolution.

Repeating this same process in the presence of an additional magnetic field  $H_z$  allows us to map out the full magnetic field response of the sample, as shown in the colour plot of Fig. 3b. In these wide and long ( $L > \lambda_F$ ) JJs, the supercurrent per unit width  $j_s$  is given by  $j_s = j_c(H_x) \sin(\Delta\phi(x))$ , where  $j_c$  is the Josephson critical-current density (ref. 26). Applying a perpendicular field  $H_z$  results in the usual Fraunhofer response due to the position dependence of  $\Delta\phi(x)$  along  $W$ . The Zeeman effect due to  $H_x$  directly affects the amplitude of  $j_c$ . For a sufficiently strong  $H_x$ , it can even reverse the sign of  $j_c$ , inducing a  $\pi$  phase shift. In this picture, the clearly visible first and second re-entrance nodes at  $H_x \approx 60$  and 200 mT, which are roughly independent of  $H_z$ , suggest exactly such an amplitude modulation of  $j_c(H_x)$  due to a spatial modulation of the pFLO order parameter<sup>8–10</sup>. It should be noted that, to acquire these data, great care has to be taken to precisely identify the plane of the sample with respect to the magnetic field directions (see Supplementary Section 2D for further detail). This is essential given that, to reveal the interesting structure in both directions, the field range of  $H_x$  needs to be about 1,000 times that of  $H_z$ , such that a mis-alignment of even  $1^\circ$  would lead to a noticeable distortion of the data.

As discussed above, to unambiguously determine the existence of the pFLO character of the state in the presence of  $H_x$ , one must examine the temperature dependence of  $I_C$ . When no in-plane field  $H_x$  is applied, as shown in Fig. 4a, the critical current decreases monotonically with increasing temperature. However, when  $H_x$  is increased,  $I_C$  at the base temperature starts to reduce, effectively vanishing at 60 mT, as shown

by the thicker curve in Fig. 4a (and consistent with Fig. 3b). With a further increase in  $H_x$  up to 100 mT, the critical current at the base temperature  $I_C(T = 25$  mK) increases and the temperature at which the zero critical current feature is observed also increases. This non-monotonic temperature dependence at finite  $H_x$  can be clearly seen in the colour plot of Fig. 4b, which shows the differential resistance ( $dV/dI$ ) extracted from  $I(V)$  curves taken for the case of  $H_x = 85$  mT plotted as a function of the current through the junction and temperature. The dark-blue area is the zero resistance region, while the paler colours show the resistive state. Clearly, also this temperature dependence shows a 0– $\pi$  transition, at a temperature of about 400 mK. Since the non-monotonic behaviour in  $I_C$  occurs only in the presence of finite in-plane magnetic field, the re-entrant behaviour in the weak link must be driven by a Zeeman-energy-like term. This is in contrast to the situation in ref. 17, where related in-plane re-entrance effects in HgTe not doped with Mn could be attributed to Rashba spin–orbit coupling effects.

To better understand the role of the Zeeman energy, we convert the data from Fig. 4a to a two-dimensional diagram of  $I_C(H_x, T)$  with respect to field and temperature. This plot is shown in Fig. 5a for the  $L = 950$  nm junction J2, whereas Fig. 5b shows a similar plot for J1 ( $L = 730$  nm). In these figures, the supercurrent is normalized to its value at zero field and base temperature, and the zero critical current nodes are identified by the dark-green colour. Both junctions show qualitatively the same behaviour: at the lowest temperature, the first node moves towards lower magnetic field. This observation can be explained by the temperature and field dependence of the effective average magnetization of the Mn atoms in the weak link. The alignment of the moments of the magnetic doping atoms in response to a magnetic field in dilute magnetic semiconductors is known to lead to a giant

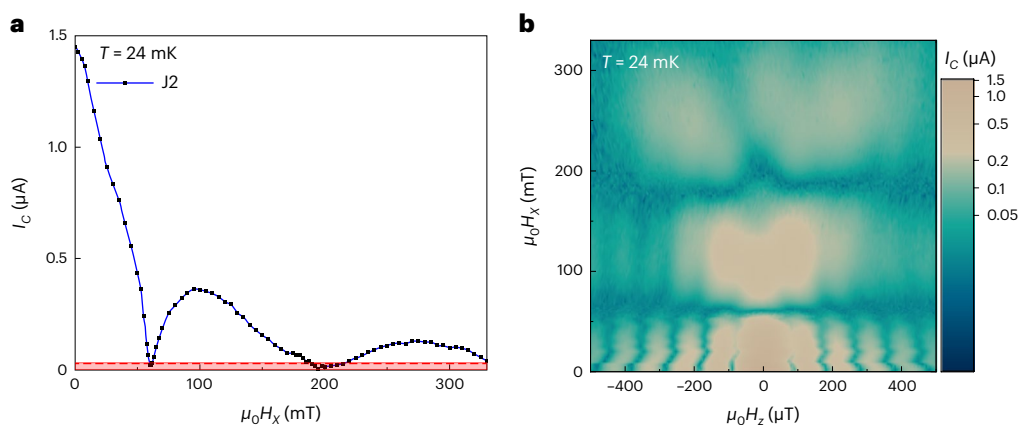


**Fig. 3 | The magnetic field dependence of the critical current.** **a**,  $I_C$  versus applied  $H_x$  at zero perpendicular-to-plane field. **b**, A colour plot of  $I_C$  as a function of  $H_z$  and  $H_x$ . The measurements were done at the base temperature of the dilution fridge on junction J2.

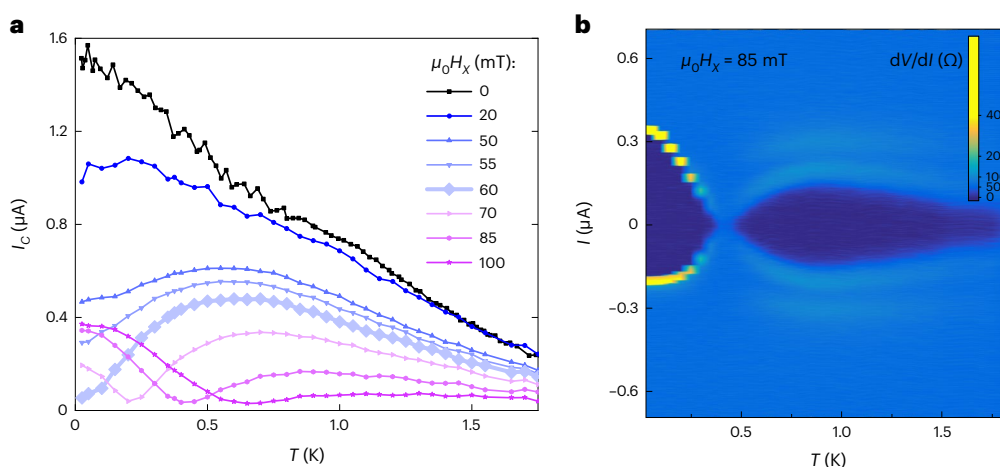


**Fig. 4 | The magnetic field and temperature dependence of critical current.** **a**, The temperature dependence of  $I_C$  at different  $H_x$ . **b**, A colour plot of  $dV/dI$  versus current and temperature for  $H_x = 85$  mT.

effective Zeeman effect, mediated through the exchange interaction between the  $d$  orbitals of Mn and the  $s$ - $p$  orbitals of the current carrier electrons. The effective Zeeman energy ( $E_Z^*$ ) in this case follows the modified Brillouin function ( $B_{5/2}$ ) for spin  $5/2$  (refs. 28–30), given by

$$E_Z^* = g_0 \mu_B \mu_0 H - \Delta E_{\max} B_{5/2} \left[ \frac{S g_{\text{Mn}} \mu_B \mu_0 H}{2 k_B (T + T_0)} \right], \quad (1)$$

where  $g_0 = -20$  is the  $g$  factor for a HgTe quantum well without Mn atoms<sup>31</sup>,  $\mu_B$  is the Bohr magneton,  $\mu_0$  is the vacuum magnetic permeability,  $g_{\text{Mn}} = 2$  is the  $g$  factor for the  $\text{Mn}^{2+}$  ion,  $T$  is the temperature of the Mn spin system and  $k_B$  is the Boltzmann constant. For (Hg, Mn)Te with a Mn concentration of 2.3%,  $\Delta E_{\max} = 4.3$  meV is the saturated spin-splitting energy due to the  $sp$ - $d$  exchange interaction<sup>29,30</sup> and  $T_0 = 730$  mK (refs. 22–25) is an empirical fitting parameter that phenomenologically accounts for the antiferromagnetic coupling between neighbouring Mn spins or to Mn clusters with non-zero spin<sup>32</sup> (for a detailed discussion of this choice of parameters, see Supplementary Section 2F). Because of the argument of the Brillouin function, as the temperature is reduced, maintaining a constant  $E_Z^*$  requires also reducing the magnetic field. This explains the reduction in the magnetic field required to observe the re-entrance behaviour at the lowest temperatures of Fig. 5a,b.

To analyse the impact of the large Zeeman splitting on the transport, we adapt the model of ref. 33 for the case of magnetic dopants

(see Supplementary Section 1 for details). In the clean limit, the critical current is given by equation (20) of ref. 33. This is modified to our case by equating the exchange field in the ferromagnet to the effects of giant Zeeman splitting and can thus be rewritten as

$$I_C \propto T \left| \sum_{\omega > 0}^{\infty} f_s^2 \gamma^2 \frac{\sin(2E_Z^* L / \hbar v_F)}{2E_Z^* L / \hbar v_F} e^{-\frac{L}{\tau}(1+2\omega\tau)} \right|. \quad (2)$$

This equation then describes the dependence of the critical current on temperature and  $E_Z^*$ . The summation is over the Matsubara frequency (where  $\hbar\omega_n = \pi k_B T(2n + 1)$  with  $n = 0, 1, 2, \dots$ ).  $v_F = 6.3 \times 10^5$  m  $s^{-1}$  is taken from the established band structure for a HgTe quantum well of this thickness and Mn concentration<sup>34</sup> and  $\tau (= l/v_F)$  is the momentum relaxation time.  $\gamma$  is an effective parameter describing the transport through the hybrid interface.  $f_s = \Delta / \sqrt{\Delta^2 + (\hbar\omega_n)^2}$  is the anomalous Green's function describing the superconducting state in the leads.

The  $\gamma$  parameter in equation (2), which can be assumed to be temperature and magnetic field independent within the experimental range, is treated as an overall normalization. By using equation (2) with the material parameters taken from the above cited literature, we can compute the  $I_C(H_x, T)/I_C(0, T_{\min})$  diagram without additional parameters. Colour plots of such simulations are shown in Fig. 5c,d for each of the two junctions and show reasonable agreement with the data in Fig. 5a,b. Furthermore, the simulation can be compared with the

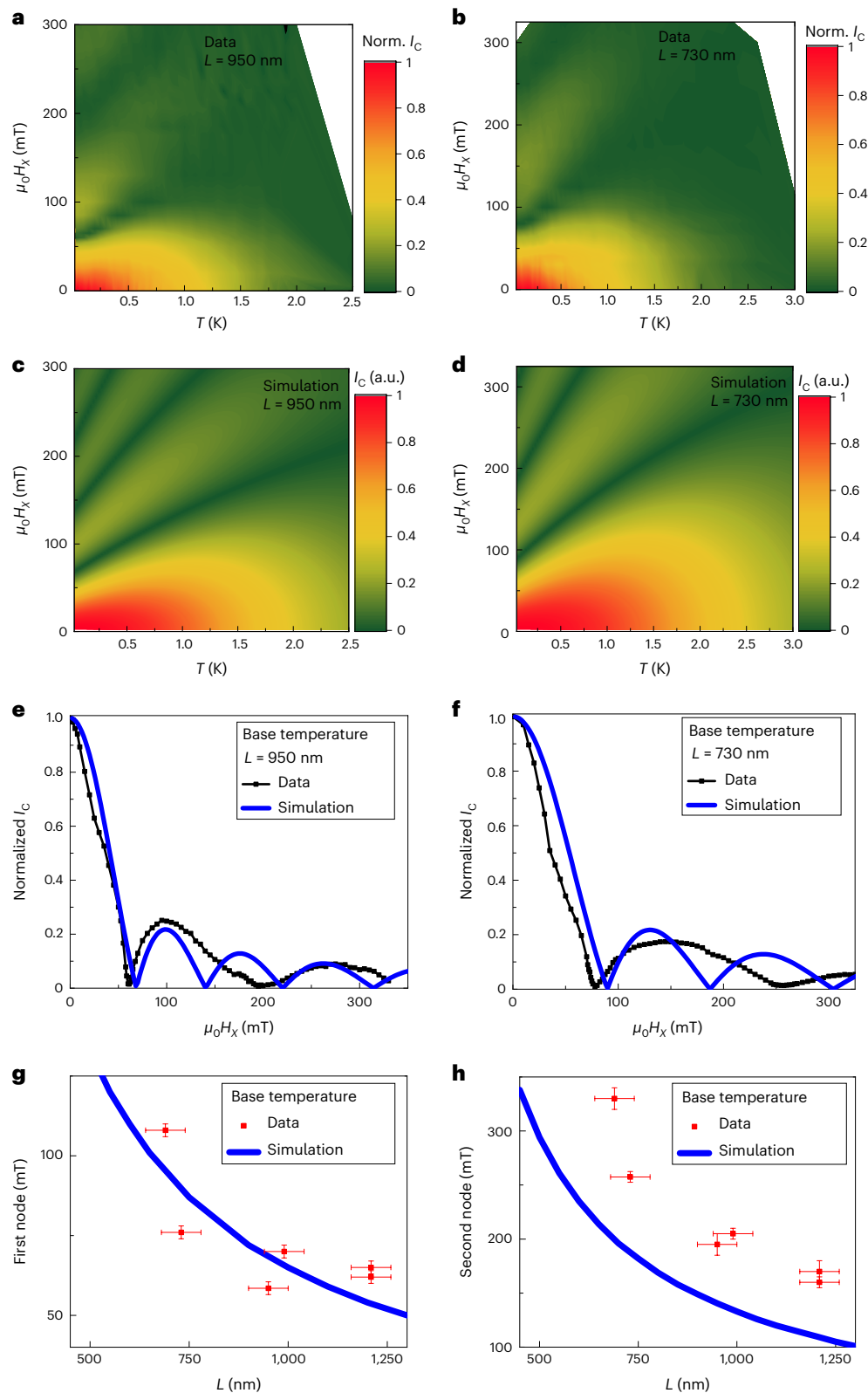


**Fig. 5 | Comparing experiment and theory.** **a, b,** A colour plot of the normalized  $(\text{Norm.}) I_c(H_x, T)$  for a JJ of  $L = 950$  nm (**a**) and  $730$  nm (**b**). **c, d,** A simulation of  $I_c(H_x, T)$  for a JJ of  $L = 950$  nm (**c**) and  $730$  nm (**d**). **e, f,** The base-temperature-normalized  $I_c(H_x)$  along with a simulation for the JJs of length  $950$  and  $730$  nm, respectively. **g,** First and (**h**) second re-entrance nodes for JJs with varied  $L$  at

the base temperature along with the extracted node from the simulation. The length of the junctions is determined from optical microscope images of the finished samples and has an uncertainty of less than  $50$  nm (limited by pixel size). The y-axis error bar estimates the reading uncertainty on the position of the re-entrance nodes.

experimental data by looking at the normalized  $I_c$  at the base temperature with respect to  $H_x$  (Fig. 5e,f). The simulation reasonably well reproduces the position of nodes in magnetic field for both lengths  $L$  of junctions. The length of the junctions is determined from optical microscope images of the finished samples and has an uncertainty of less than 50 nm (limited by pixel size), whereas the y-axis error bar estimates the reading uncertainty on the position of the re-entrance nodes. The simulation captures not only the position of the nodes but also the amplitude of the re-entrant supercurrent at higher fields. As an additional comparison, in Fig. 5g,h, we look at the field position of the first and second node for the six studied devices, as a function of device length, again showing that the simulation correctly captures the experimental observations. Taken as a whole, the agreement between the experiment and equation (2) highlighted in Fig. 5 indicates the Zeeman-driven pFLO nature of the state responsible for the re-entrant superconductivity. To capture any influence of Rashba-type spin-orbit coupling in the low field re-entrant superconductivity would require more detailed studies. Indeed, the agreement is surprisingly good given that equation (2) assumes  $E_Z^* > \hbar/\tau$ , which is satisfied for fields much higher than 24 mT. Equation (1) is empirically well established for temperatures greater than  $T_0$  and appears to work quite well here despite the fact that applying the equation well below  $T = T_0$  is pushing the range of its tested validity.

Note that a conceptually similar model developed by Pientka et al.<sup>35</sup> was applied by Hart et al.<sup>17</sup> to describe their data on a non-magnetic weak link. In the Pientka model, the considered problem is fully one dimensional, with only the current trajectory orthogonal to the JJ width taken into account. This model is sufficient to explain the set of data accessible in Hart et al. and indeed also can explain some features of our data such as the magnetic field at which minima in  $I_c$  occur. Our probe of higher magnetic fields reveals features such as the magnetic field and temperature dependence of  $I_c$  in the re-entrant lobes, which are not captured in this one-dimensional picture. In the same spirit, equation (2) takes the finite width of the JJ into account by averaging over the distribution of possible injection angles and reveals the rich physics allowing us to identify FFLO behaviour.

## Conclusion

Whereas the FFLO state is determined by the properties of the bulk superconductor, the proximity-induced version of the effect depends on the properties of the weak link, which, as shown here, can be a semiconductor. Given the relative ease with which the transport properties of semiconductors (as opposed to those of metals) are affected by magnetic and electric fields as well as currents, this platform provides the flexibility to explore FFLO physics in ways that were previously experimentally inaccessible.

## Online content

Any methods, additional references, Nature Portfolio reporting summaries, source data, extended data, supplementary information, acknowledgements, peer review information; details of author contributions and competing interests; and statements of data and code availability are available at <https://doi.org/10.1038/s41567-024-02477-1>.

## References

- Fulde, P. & Ferrell, R. A. Superconductivity in a strong spin-exchange field. *Phys. Rev.* **135**, A550–A563 (1964).
- Larkin, A. & Ovchinnikov, Y. N. Nonuniform state of superconductors. *Sov. Phys. JETP* **20**, 762–770 (1965).
- Singleton, J. et al. Observation of the Fulde–Ferrell–Larkin–Ovchinnikov state in the quasi-two-dimensional organic superconductor  $\kappa$ -(BEDT-TTF)<sub>2</sub>Cu(NCS)<sub>2</sub> (BEDT-TTF=bis(ethylene-dithio)tetrathiafulvalene). *J. Phys. Condens. Matter* **12**, L641–L648 (2000).
- Zhao, H. et al. Smectic pair-density-wave order in EuRbFe<sub>4</sub>As<sub>4</sub>. *Nature* **618**, 940–945 (2023).
- Liu, Y. et al. Pair density wave state in a monolayer high- $T_c$  iron-based superconductor. *Nature* **618**, 934–939 (2023).
- Aishwarya, A. et al. Magnetic-field-sensitive charge density waves in the superconductor UTe<sub>2</sub>. *Nature* **618**, 928–933 (2023).
- Gu, Q. et al. Detection of a pair density wave state in UTe<sub>2</sub>. *Nature* **618**, 921–927 (2023).
- Demler, E. A., Arnold, G. & Beasley, M. Superconducting proximity effects in magnetic metals. *Phys. Rev. B* **55**, 15174–15182 (1997).
- Buzdin, A. I. Proximity effects in superconductor-ferromagnet heterostructures. *Rev. Mod. Phys.* **77**, 935–976 (2005).
- Bergeret, F., Volkov, A. F. & Efetov, K. B. Odd triplet superconductivity and related phenomena in superconductor-ferromagnet structures. *Rev. Mod. Phys.* **77**, 1321–1373 (2005).
- Ryazanov, V. et al. Coupling of two superconductors through a ferromagnet: evidence for a  $\pi$  junction. *Phys. Rev. Lett.* **86**, 2427–2430 (2001).
- Kontos, T. et al. Josephson junction through a thin ferromagnetic layer: negative coupling. *Phys. Rev. Lett.* **89**, 137007 (2002).
- Sellier, H., Baraduc, C., Lefloch, F. & Calemczuk, R. Temperature-induced crossover between 0 and  $\pi$  states in S/F/S junctions. *Phys. Rev. B* **68**, 054531 (2003).
- Frolov, S., Van Harlingen, D., Oboznov, V., Bolginov, V. & Ryazanov, V. Measurement of the current–phase relation of superconductor/ferromagnet/superconductor  $\pi$  Josephson junctions. *Phys. Rev. B* **70**, 144505 (2004).
- Robinson, J., Witt, J. & Blamire, M. Controlled injection of spin-triplet supercurrents into a strong ferromagnet. *Science* **329**, 59–61 (2010).
- Gingrich, E. et al. Controllable 0– $\pi$  Josephson junctions containing a ferromagnetic spin valve. *Nat. Phys.* **12**, 564–567 (2016).
- Hart, S. et al. Controlled finite momentum pairing and spatially varying order parameter in proximitized HgTe quantum wells. *Nat. Phys.* **13**, 87–93 (2017).
- Ke, C. T. et al. Ballistic superconductivity and tunable  $\pi$ -junctions in InSb quantum wells. *Nat. Commun.* **10**, 3764 (2019).
- Dartiailh, M. C. et al. Phase signature of topological transition in Josephson junctions. *Phys. Rev. Lett.* **126**, 036802 (2021).
- Dvir, T. et al. Planar graphene–NbSe<sub>2</sub> Josephson junctions in a parallel magnetic field. *Phys. Rev. B* **103**, 115401 (2021).
- Das, B. et al. Evidence for spin splitting in In<sub>x</sub>Ga<sub>1-x</sub>As/In<sub>0.52</sub>Al<sub>0.48</sub>As heterostructures as  $B \rightarrow 0$ . *Phys. Rev. B* **39**, 1411–1414 (1989).
- Twardowski, A., Von Ortenberg, M., Demianiuk, M. & Pauthenet, R. Magnetization and exchange constants in Zn<sub>1-x</sub>Mn<sub>x</sub>Se. *Solid State Commun.* **51**, 849–852 (1984).
- Yu, W., Twardowski, A., Fu, L., Petrou, A. & Jonker, B. Magnetoanisotropy in Zn<sub>1-x</sub>Mn<sub>x</sub>Se strained epilayers. *Phys. Rev. B* **51**, 9722–9727 (1995).
- Twardowski, A., Swiderski, P., Von Ortenberg, M. & Pauthenet, R. Magnetoabsorption and magnetization of Zn<sub>1-x</sub>Mn<sub>x</sub>Te mixed crystals. *Solid State Commun.* **50**, 509–513 (1984).
- Gaj, J., Planel, R. & Fishman, G. Relation of magneto-optical properties of free excitons to spin alignment of Mn<sup>2+</sup> ions in Cd<sub>1-x</sub>Mn<sub>x</sub>Te. *Solid State Commun.* **29**, 435–438 (1979).
- Tinkham, M. *Introduction to Superconductivity* 2nd edn (Dover, 2004).
- Mandal, P. et al. Finite field transport response of a dilute magnetic topological insulator-based Josephson junction. *Nano Lett.* **22**, 3557–3561 (2022).
- Brandt, N. & Moshchalkov, V. V. Semimagnetic semiconductors. *Adv. Phys.* **33**, 193–256 (1984).

29. Gui, Y. et al. Interplay of Rashba, Zeeman and Landau splitting in a magnetic two-dimensional electron gas. *Europhys. Lett.* **65**, 393–399 (2004).
30. Novik, E. et al. Band structure of semimagnetic  $\text{Hg}_{1-y}\text{Mn}_y\text{Te}$  quantum wells. *Phys. Rev. B* **72**, 035321 (2005).
31. Zhang, X. C., Ortner, K., Pfeuffer-Jeschke, A., Becker, C. R. & Landwehr, G. Effective  $g$  factor of  $n$ -type  $\text{HgTe}/\text{Hg}_{1-x}\text{Cd}_x\text{Te}$  single quantum wells. *Phys. Rev. B* **69**, 115340 (2004).
32. Twardowski, A., Dietl, T. & Demianiuk, M. The study of the  $s$ - $d$  type exchange interaction in  $\text{Zn}_{1-x}\text{Mn}_x\text{Se}$  mixed crystals. *Solid State Commun.* **48**, 845–848 (1983).
33. Bergeret, F., Volkov, A. & Efetov, K. Josephson current in superconductor-ferromagnet structures with a nonhomogeneous magnetization. *Phys. Rev. B* **64**, 134506 (2001).
34. Shamim, S. et al. Emergent quantum Hall effects below 50 mT in a two-dimensional topological insulator. *Sci. Adv.* **6**, eaba4625 (2020).
35. Pientka, F. et al. Topological superconductivity in a planar Josephson junction. *Phys. Rev. X* **7**, 021032 (2017).

**Publisher's note** Springer Nature remains neutral with regard to jurisdictional claims in published maps and institutional affiliations.

**Open Access** This article is licensed under a Creative Commons Attribution 4.0 International License, which permits use, sharing, adaptation, distribution and reproduction in any medium or format, as long as you give appropriate credit to the original author(s) and the source, provide a link to the Creative Commons licence, and indicate if changes were made. The images or other third party material in this article are included in the article's Creative Commons licence, unless indicated otherwise in a credit line to the material. If material is not included in the article's Creative Commons licence and your intended use is not permitted by statutory regulation or exceeds the permitted use, you will need to obtain permission directly from the copyright holder. To view a copy of this licence, visit <http://creativecommons.org/licenses/by/4.0/>.

© The Author(s) 2024

## Methods

### Quantum well growth and properties

The weak link is composed of a 2.3% Mn-doped 11-nm-thick (Hg, Mn) Te quantum well sandwiched between (Hg, Cd)Te layers, grown by molecular beam epitaxy. These parameters place the quantum well in the topological regime<sup>34</sup>. This, however, does not play a role in the results of this paper since these devices are all highly  $n$  doped. The carrier density and mobility are  $8.8 \times 10^{11} \text{ cm}^{-2}$  and  $111,000 \text{ cm}^2 \text{ Vs}^{-1}$ , respectively, as determined from measurements on a  $180 \times 540 \mu\text{m}$  Hall bar made from the same wafer. This density corresponds to a Fermi wavelength  $\lambda_F = 27 \text{ nm}$  and a Fermi energy ( $E_F$ ) of 97 meV above the bottom of the conduction band in our devices.

### Lithography and measurement technique

The weak-link mesa is patterned using wet-etch techniques<sup>36</sup>. The geometry and technology used to produce the JJs are the same as in ref. 27. Direct current  $I(V)$  measurements are performed using a quasi-four-probe configuration where the current is swept from negative to positive values for all the data presented here.

### Data availability

All data needed to evaluate the conclusions in the paper are present in the paper and/or Supplementary Information. Additional data related to this paper may be requested from the authors. Source data are provided with this paper.

## References

36. Bendias, K. et al. High mobility HgTe microstructures for quantum spin Hall studies. *Nano Lett.* **18**, 4831–4836 (2018).

## Acknowledgements

We thank L. Lunczer for the molecular beam epitaxy growth of the quantum well heterostructure and W. Beugeling for assistance with band structure calculation. F.S.B. thanks the Alexander von Humboldt Foundation and B. Trauzettel for their kind hospitality at the Theoretical Physics IV Institute of the Würzburg University. The work at Würzburg was supported by the ENB Graduate school on 'Topological

Insulators' (L.W.M.), the EU ERC-AG Program (project 4-TOPS) (L.W.M.), the Free State of Bavaria (the Institute for Topological Insulators) (L.W.M.), Deutsche Forschungsgemeinschaft (SFB 1170, 258499086) (M.P.S., C.G. and L.W.M.) and the Würzburg-Dresden Cluster of Excellence on Complexity and Topology in Quantum Matter (EXC 2147, 39085490) (L.W.M.). The work of the San Sebastian group was supported by the Spanish AEI through projects PID2020-114252GB-I00 (SPIRIT) (F.S.B.) and TED2021-130292B-C42 (F.S.B.) and the European Union's Horizon 2020 Research and Innovation Framework Programme under grant no. 800923 (SUPERTED) (F.S.B.).

## Author contributions

M.P.S., C.G. and L.W.M. conceived and planned the experiment. P.M. fabricated the devices. P.M., M.P.S. and C.G. executed the measurements. S.I. and F.S.B. did the theoretical modelling. All authors contributed to discussion, analysis and understanding of the results and participated in the preparation of the manuscript.

## Funding

Open access funding provided by Julius-Maximilians-Universität Würzburg.

## Competing interests

The authors declare no competing interests.

## Additional information

**Supplementary information** The online version contains supplementary material available at <https://doi.org/10.1038/s41567-024-02477-1>.

**Correspondence and requests for materials** should be addressed to Pankaj Mandal, Charles Gould or Laurens W. Molenkamp.

**Peer review information** *Nature Physics* thanks the anonymous reviewer(s) for their contribution to the peer review of this work.

**Reprints and permissions information** is available at [www.nature.com/reprints](http://www.nature.com/reprints).